Journal of Materials Chemistry C

ROYAL SOCIETY OF CHEMISTRY

PAPER

View Article Online
View Journal | View Issue

Cite this: J. Mater. Chem. C, 2022, 10, 14344

Biaxial strain induced multiple magnetic phase transitions in nonmagnetic transition metal halide monolayer

Jun Zhou, [a] Xiaoguang Xu,[b] Tong Yang,[c] Jingyu He,[c] Jianwei Chai,[a] Lai Mun Wong,[a] Yuan Ping Feng, [de] Ming Yang, *[c] Lei Shen *[f] and Shijie Wang *[a]

Two-dimensional (2D) materials are sensitive to external stimuli. In this work, *via* a combined first-principles simulations and constrained random phase approximation, we report strain-induced multiple magnetic phase transitions in an exfoliable nonmagnetic metallic 2D material ScI_2. Interestingly, monolayer ScI_2 has a high density of states at the Fermi level [$N(E_F)$]. Its product with the Stoner parameter is estimated to be slightly below the critical value of the Stoner criterion for spontaneous spin splitting. Moreover, we show bi-axial strains can effectively increase the $N(E_F)$ of ScI_2, leading to phase transitions to magnetic states. While the tensile strain first yields an antiferromagnetic state at the critical magnitude of 3%, then a normal ferromagnetic state at 5%, and half-metallicity with large spin flip gaps for the minority spins for strains $\geq$ 6%, compressive strain induces a ferromagnetic configuration ranging from −6% to −10%. Our results demonstrate a system with strain controllable magnetic states, appealing for straintronic and spintronic applications, and provide guidance on the design of extrinsic 2D magnetic materials.

Received 4th August 2022,
Accepted 5th September 2022

DOI: 10.1039/d2tc03268f

rsc.li/materials-c

Introduction

Two-dimensional (2D) materials naturally have a wide spectrum of fascinating properties. For example, their pure surfaces yield super-high surface-volume ratios, which are ideal for high-performance catalysts;[1] they are inherent nanomaterials for high-density integration;[2] the van der Waals interaction between 2D materials enables them as blocking units for more complex structures, including morié patterns[3] and van der Waals heterostructures.[4] In particular, 2D materials are intrinsically capable of withstanding strong deformation compared with bulk materials.[5] In addition, their atomic-scale thickness allows various methods to induce large local strains.[6,7] More importantly, strain engineering has been demonstrated to effectively change the various physical properties of 2D materials from carrier mobility,[8] phonon modes,[9,10] optical responses[11] to magnetic properties.[12,13] Such controllable manipulation of physical properties is appealing for strain-assisted device functionalities, including sensing, data storing, computing, and logic operation for next-generation flexible and wearable electronics.[6,7] Due to the rich physics and practical applications, a new research area called 'straintronics' emerges in condensed matter physics, especially for 2D materials.[14,15]

Besides, two-dimensional magnetism has attracted tremendous research interest ever since the experimental reports of true 2D magnets.[16,17] Unfortunately, most 2D materials are nonmagnetic, and the intrinsic 2D magnetic materials are rare. Therefore, extrinsic methods to induce magnetism in nonmagnetic 2D materials also have been actively explored. The reported successes in this regard mainly focus on the following directions:[18] (a) adding adatoms such as hydrogen atoms;[19] (b) flat band ferromagnetism from nanoribbon edges or grain boundaries of 2D materials;[20–22] (c) Fermi level shifting by carrier doping[23] and (d) magnetic proximity effect.[24,25] Strain engineering has been demonstrated to stabilize the magnetism of either extrinsic or intrinsic 2D magnetic materials,[26–29] but the pure strain-induced magnetism in nonmagnetic 2D materials is less studied.

In this work, *via* first-principles calculations, we studied the strain effects on a stable nonmagnetic metallic 2D material, T-phase ScI_2,

[a] *Institute of Materials Research & Engineering, A*STAR (Agency for Science, Technology and Research), 2 Fusionopolis Way, Innovis, Singapore 138634, Singapore. E-mail: sj-wang@imre.a-star.edu.sg*
[b] *School of Materials Science and Engineering, University of Science and Technology Beijing, Beijing, 100083, China*
[c] *Department of Applied Physics, The Hong Kong Polytechnic University, Hung Hom, Kowloon, Hong Kong SAR, China. E-mail: mingyang@polyu.edu.hk*
[d] *Department of Physics, National University of Singapore, Singapore 117551, Singapore*
[e] *Center for Advanced Two-Dimensional Materials (CA2DM), National University of Singapore, Singapore 117546, Singapore*
[f] *Department of Mechanical Engineering, National University of Singapore, Singapore 117575, Singapore. E-mail: shenlei@nus.edu.sg*

which can be potentially exfoliated from its parent layered bulk. Our results show that this system undergoes rich magnetic phase transitions by tensile strains: from nonmagnetic to antiferromagnetic (AFM) configuration at 3%, then a transition to ferromagnetic (FM) state at 5% and becoming half-metal after 6% of tensile strain. We have systematically evaluated the Stoner criterion for monolayer ScI_2 under various strains and found that it can well explain the onset of magnetism in this system. These results demonstrate strain engineering as an effective way to manipulate the magnetic properties of 2D materials and provide insight into the underlying mechanisms.

Methods

All the density functional theory (DFT) calculations were performed by Vienna *ab initio* Simulation Package (VASP)[30,31] with the Perdew–Burke–Ernzerhof (PBE) approximation for the exchange-correlation functional, and the frozen-core all-electron projector augmented wave (PAW) method for the electron-ion interaction.[32] The plane wave expansion was well converged at a cutoff energy of 420 eV. A Γ-centered $31 \times 31 \times 1$ k-point grid was used to sample the reciprocal space. The structures were fully relaxed until the energy and force were converged to 10^{-6} eV and 0.001 eV $Å^{-1}$, respectively. The thickness of the vacuum layer was set to around 30 Å to eliminate the interaction between the images resulting from the periodic boundary condition. The exfoliation energy was estimated by the difference of the total energy per atom between 2D and bulk structures, both of which are corrected by Grimme's DFT-D3 scheme.[33] The energy above the hull is obtained by constructing a phase diagram by competing phases queried from the Materials Project database.[34] Phonon dispersions were calculated by finite displacement approach with a $2 \times 2 \times 1$ supercell.[35] The Wannier function was constructed from the results of the DFT calculations using the procedure of maximal localization by the Wannier90 package as implemented in VASP.[36] The maximally-localised Wannier functions (MLWFs) have been constructed from the t_{2g} orbitals for the three bands around the Fermi level, which have been used for further constrained random phase approximation (cRPA) calculations to obtain the screened Coulomb interaction matrix.[37,38]

Results and discussion

Fig. 1(a) shows the structure of the monolayer ScI_2, in which the Sc atoms in the middle layer are octahedrally coordinated with the top and bottom I atoms with a space group of $P\bar{3}m1$, resembling a T-phase MoS_2.[39] In the following, all the materials discussed in this work are in the specific T phase unless otherwise stated. The optimized in-plane lattice parameter of ScI_2 (4.04 Å) is much larger than that of the T-phase MoS_2 (3.18 Å), both of which are calculated by the same PBE level in VASP.[39] It is noted that the bulk layered ScI_2 in the 1T phase has been experimentally synthesized.[40] The estimated exfoliation

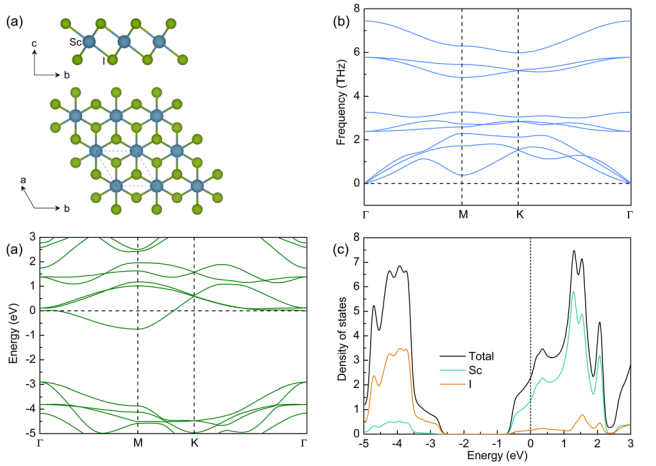

Fig. 1 (a) Side and top view of the structure, (b) phonon spectra, (c) band structure, and (d) projected density of states for monolayer ScI_2 in T phase. The Fermi energy is aligned to 0 eV in (c) and (d).

energy of monolayer ScI_2 is 73 meV per atom (15 meV $Å^{-2}$), which is comparable with that of graphene (66 meV per atom),[41] and is within the range for the easily exfoliable compounds.[41,42] Its thermodynamic stability is confirmed by its energy above the hull of 0 meV per atom. It is noted that its layered parent bulk is not included in the phase diagram to obtain the hull curve. Besides, the phonon spectra of monolayer ScI_2 are free of imaginary frequencies [see Fig. 1(b)], demonstrating its dynamic stability, which is in contrast with the heavy phonon softening of the T-phase MoS_2.

The electronic properties of monolayer ScI_2 are further studied. From the band structure shown in Fig. 1(c), the monolayer ScI_2 is nonmagnetic and metallic. There are three bands around the Fermi level, and another two separated by a gap at a higher energy level. These are the typical octahedral crystal-field splitting of the 3d orbitals of Sc atoms into lower three-fold degenerate t_{2g} bands and higher two-fold degenerate e_g bands. The one electron from the 3d orbital of the Sc ion partially occupies the degenerate t_{2g} bands, leading to a metallic behavior. It is interesting to note that the t_{2g} bands in monolayer ScI_2 have a much smaller bandwidth (around 1.9 eV) than that of T-phase MoS_2 (around 3.6 eV),[39] which can be understood by that these bands are contributed by the more localized 3d orbitals of Sc in ScI_2 than the 4d orbitals of Mo in MoS_2 as well as the much larger in-plane lattice parameters of ScI_2 than MoS_2 monolayer.

Accordingly, the density of states (DOS) around the Fermi level is mainly contributed by Sc ions [see Fig. 1(d)]. Remarkably, the total DOS at the Fermi level of the monolayer ScI_2 is relatively high (2.3 states per eV). This value is much larger than that of MoS_2[39] and comparable with that of VS_2,[43] the latter of which undergoes spontaneous spin splitting and is ferromagnetic.[44] According to the Stoner model, this might suggest that the monolayer ScI_2 is on the verge of magnetic instability.[45] This further motivates us to explore the possibility of inducing a magnetic phase for the monolayer ScI_2 by external stimuli. In this work, we choose strain engineering, which is suitable to manipulate the properties of

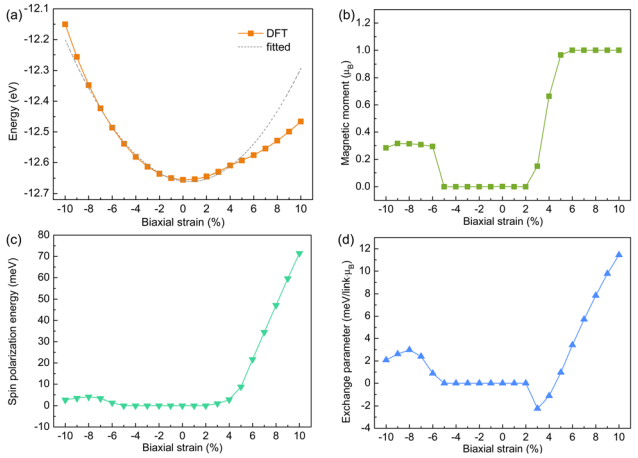

Fig. 2 In-plane biaxial strain-dependent (a) total energy, (b) total magnetic moment, (c) spin polarization energy, and (d) magnetic exchange parameter for monolayer ScI_2. The dotted curve in (a) is a quadratic fitting of the energies under −10% to 4% strains as a guidance of the eye.

monolayer ScI_2 because it has been shown to modulate various properties of 2D materials effectively.

The strain-dependent electronic and magnetic properties of the monolayer ScI_2 are summarized in Fig. 2. As shown by the total energy of the material under each strain in Fig. 2(a), both compressive and tensile in-plane strain increase the total energy of the system, forming a parabola shape. However, there are deviations in the range of larger than 4% tensile strains, in which the total energies are lower than the fitted parabola curve, implying that the system undergoes a phase transition. Indeed, as shown in Fig. 2(b), the monolayer ScI_2 becomes magnetic at 3% of tensile strain. The total magnetic moment of the system further increases with the strain strength and converges at 1 μ_B per formula unit (f.u.) at 6% of tensile strain. Considering there is only one electron occupying the t_{2g} bands, the 1 μ_B magnetic moment under the larger tensile strains (>6%) suggests the full spin polarization of this electron and a half-metallic nature of the system. Interestingly, compressive strains also induce magnetic moments to ScI_2 but in a step-like manner with a sudden increase of a total magnetic moment of around 0.3 μ_B per f.u. at the magnitude of 6% and a plateau to the maximum compressive strain studied in this work.

The strength of the exchange coupling between the magnetic moments is further studied by comparing the energies between the ferromagnetic and antiferromagnetic configurations for the magnetic systems. As shown in Fig. 2(d), the exchange parameters are negative for 3% and 4% tensile strains, implying an antiferromagnetic ordering for these two cases. Beyond 4%, the exchange parameter increases monotonically with the tensile strain. The system becomes ferromagnetic at 5% of tensile strain, and the FM coupling is increasingly stronger with the tensile strain. This metal-metal distance dependent AFM-to-FM transition can be understood by the so-called Bethe–Slater curve.[46,47] A different pattern is shown for the system under compressive strains. Compressive strains lead to only ferromagnetic couplings, and the magnetic exchange strength is enhanced from 6% to 8% but drops after 8%.

The stability of the magnetic state under each strain is estimated by the spin polarization energy, which is defined as the energy difference between the nonmagnetic state and the ferromagnetic or antiferromagnetic state, depending on which is the ground-state magnetic configuration. A positive value suggests that the magnetic state is more stable. As shown in Fig. 2(c), the monolayer ScI_2 prefers to stay in the nonmagnetic state in the range from 5% compressive and 2% tensile strains, as indicated by their negligible spin polarization energies. The magnetic state becomes the ground state at 3% tensile strain and is increasingly stable with the higher tensile strain strength. On the contrary, under the compressive strain, the system starts to prefer a magnetic state at 6%, but the spin polarization energies are more or less constant (around 5 meV per f.u.) in the larger strain range.

The origin of magnetic phase transition is understood by the Stoner criterion, which is evaluated by the product of the density of states for Sc at Fermi level $[N(E_F)]$ and the Stoner parameter $[I]$.[45] The strain effects on the profile of DOS around Fermi level are shown in Fig. 3(a), with the system under ±3%, 0% and ±6% bi-axial strains as representative examples. Overall, the tensile strain increases the $N(E_F)$ monotonically, which can be understood by the fact that the t_{2g} orbitals are more localized when the inter-atom distances increase with the tensile strain. Similarly, the $N(E_F)$ is expected to decrease with the compressive strains. This can be seen from the fact that the DOS under −3% and −6% is smaller than that of the pristine ScI_2 for the most part of the energy range between −1.0 eV and 1.0 eV. However, the DOS profile under compressive becomes more uneven, and the Fermi level passes through one of the developed peaks, resulting in an increase of $N(E_F)$.

For quantitative analysis, we perform cRPA simulations for the three-fold degenerate t_{2g} bands and calculate the screened Coulomb interaction matrix. The simulated Hubbard U and J are 2.82 eV and 0.28 eV, respectively. Then, the Stoner parameter is calculated by the following equation.[48]

$$I = \frac{(U + 6J)}{5}$$

However, such an assessment has been argued to lead to an overestimation of I.[48] Taking the median (25%) between the

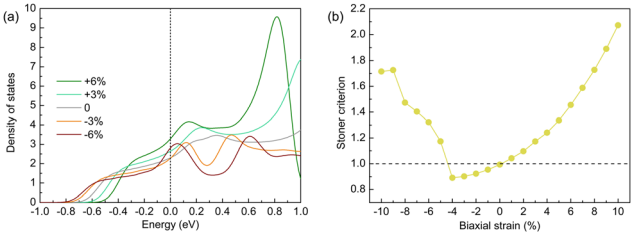

Fig. 3 In-plane biaxial strain-dependent (a) total density of states and (b) product of I and $N_{Sc}(E_F)$ of Sc for monolayer ScI_2. The Fermi energy is aligned to 0 eV in (a).

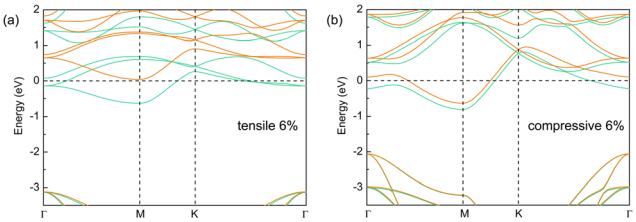

Fig. 4 Band structures for monolayer ScI_2 under (a) 6% tensile and (b) 6% compressive strains. The orange and turquoise lines represent the spin-up and spin-down bands. The Fermi energy is aligned to 0 eV.

lower (10%) and upper limits (40%) of the overestimation, we arrive at an I of 0.72 for ScI_2. And the obtained product of I and $N_{Sc}(E_F)$ of Sc ions under each bi-axial strain is shown in Fig. 3(b). Again, the tensile and compressive strains demonstrate different trends. While the $N_{Sc}(E_F) \times I$ increases monotonically with the tensile strains, under compressive strain, it decreases first from 0% to 4%, then increases more irregularly from 5% to 9%, and decreases slightly at 10% compressive strain. The smooth increase from −4% to 10% biaxial strain is likely due to the rise of $N_{Sc}(E_F)$ from the change of the distance between Sc ions by strains. The sudden jump from −4% to −5% is caused by the formation of the DOS peak at the Fermi level. More importantly, the $N_{Sc}(E_F) \times I$ is larger than 1, meeting the Stoner criterion, at the critical magnitude of 1% and 5% for the tensile and compressive strain, respectively. This overall agrees with the onset of magnetic moments at 3% tensile and 6% compressive strains, demonstrating the Stoner-type spin splitting in monolayer ScI_2.

At last, the strain effects on the electronic properties are demonstrated by the band structures of ScI_2 under the 6% tensile and 6% compressive strains as representative examples. As shown in Fig. 4(a), the spin-down channel (turquoise lines in the band structure) of the ScI_2 under 6% tensile strain is metallic while the spin-up channel (orange lines in the band structure) is insulating, indicating a half-metallicity. It is interesting to note that the spin flip energy, defined as the energy gap between the valence band maximum and Fermi energy, is 3.13 eV for the spin-up channel. This is much larger than that of most of the known half-metals such as Heusler compounds (around 100 meV).[49,50] Such a large spin flip gap for the minority spin carriers is highly desired to keep the 100% spin polarizations for the conduction electrons, ideal for next-generation spintronic devices.[51]

In contrast, the 6% compressive strain expands the t_{2g} bands to a width of around 2.6 eV, leading to their overlaps with the e_g bands. Under this condition, the spin-up and spin-down bands are split but the one valence electron still occupies both channels. Interestingly, the lowest band of the t_{2g} states shows Mexico-hat-like dispersion near the Γ point along the ΓM path [see Fig. 4(b)], in contrast to the parabolic shape under the 6% tensile strain, the former of which may be responsible for the peak around the Fermi level for the DOS under the 6% compressive strain [Fig. 3(a)].

It is noted that all the results in this work are based on the free-standing pristine ScI_2 monolayer, *i.e.*, its intrinsic properties. In experiments, the scalable growth of high-quality 2D materials remains a challenge and multiple experimental factors could significantly change the intrinsic properties of monolayers. For example, defects/contamination, which could be introduced during sample growth process such as by physical vapor deposition and liquid exfoliation as well as bottom-up chemical methods,[52,53] have been shown to change the electronic and magnetic properties of 2D materials.[54,55] Substates are also influential to the 2D crystals by exerting strains, interface interaction, *etc.*[56,57] An in-depth study of the possible extrinsic effects on ScI_2 is beyond the scope of this work. Fortunately, encouraging development of growth method for high-quality 2D materials is emerging. For example, the recently reported Au-assisted mechanical exfoliation method has been shown to be capable of growing large-area high-quality 2D materials while keeping minimal interference on the intrinsic electronic preparties of the monolayers.[58] This method is especially suitable for 2D materials with top chalcogens or halogen atoms, which might be promising to exfoliate high-quality ScI_2 monolayer.

Various experimental techniques have been used to apply strains on 2D materials including substrate effects *via* lattice mismatch or substate deformation and using scanning probe microscopy methods.[7,59,60] In particular, controllable bi-axial homogeneous strains can be applied on 2D materials by tuning the temperature of substrate with large thermal expansion thermal expansion coefficients or modulating bias voltage on piezoelectric substrates.[61–63] Similar approaches might be applicable to study the effects of bi-axial strains on the magnetic properties of ScI_2 monolayers.

Conclusions

In summary, we present a 2D system in which the magnetism is purely induced by strain engineering. Our results show that the ScI_2 monolayer can be easily exfoliated from its layered bulk, which is dynamically and thermodynamically stable. A non-magnetic to antiferromagnetic phase transition occurs in monolayer ScI_2 at 3% tensile strain, while the more stable ferromagnetic states are expected under >5% tensile strains. We further quantitatively analyze the Stoner criterion for ScI_2 under each strain and conclude that such a mechanism can nicely explain the onset of spin splitting by strain effects. Moreover, the system becomes half-metallic with a large spin flip gap for the minority spin after the tensile strain is larger than 6%. These results demonstrate the effective manipulation of the magnetic properties of 2D materials by strain engineering, promising for spintronic and straintronic applications.

Author contributions

J. Z. and X. X. contributed equally. M. Y., L. S. and S. J. W. conceived the idea. J. Z. performed the DFT calculations with the input from X. X., M. Y., L. S. and S. J. W. All authors analysed the data. J. Z. and X. X. wrote the manuscript. All

authors discussed the results and commented on the manuscript.

Conflicts of interest

There are no conflicts to declare.

Acknowledgements

This work is supported by the Ministry of Education, Singapore, under its MOE Tier 1 Awards R-144-000-441-114, R-144-000-413-114, R-265-000-691-114, and the National Natural Science Foundation of China (Grant No. 51971024). We acknowledge the computational resources supported by the National Supercomputing Centre (NSCC) Singapore and Centre of Advanced 2D Materials (CA2DM) HPC infrastructure.

References

1 B. Luo, G. Liu and L. Wang, *Nanoscale*, 2016, **8**, 6904–6920.
2 G. Fiori, F. Bonaccorso, G. Iannaccone, T. Palacios, D. Neumaier, A. Seabaugh, S. K. Banerjee and L. Colombo, *Nat. Nanotechnol.*, 2014, **9**, 768–779.
3 Y. Cao, V. Fatemi, S. Fang, K. Watanabe, T. Taniguchi, E. Kaxiras and P. Jarillo-Herrero, *Nature*, 2018, **556**, 43–50.
4 A. K. Geim and I. V. Grigorieva, *Nature*, 2013, **499**, 419–425.
5 C. Lee, X. Wei, J. W. Kysar and J. Hone, *Science*, 2008, **321**, 385–388.
6 Z. Dai, L. Liu and Z. Zhang, *Adv. Mater.*, 2019, **31**, e1805417.
7 S. Yang, Y. Chen and C. Jiang, *InfoMat*, 2021, **3**, 397–420.
8 Y. Wu, K. Xu, C. Ma, Y. Chen, Z. Lu, H. Zhang, Z. Fang and R. Zhang, *Nano Energy*, 2019, **63**, 103870.
9 T. M. G. Mohiuddin, A. Lombardo, R. R. Nair, A. Bonetti, G. Savini, R. Jalil, N. Bonini, D. M. Basko, C. Galiotis, N. Marzari, K. S. Novoselov, A. K. Geim and A. C. Ferrari, *Phys. Rev. B: Condens. Matter Mater. Phys.*, 2009, **79**, 205433.
10 D. Yoon, Y. W. Son and H. Cheong, *Phys. Rev. Lett.*, 2011, **106**, 155502.
11 K. Beach, M. C. Lucking and H. Terrones, *Phys. Rev. B*, 2020, **101**, 155431.
12 J. Zhou, X. Song, J. Chai, N. L. M. Wong, X. Xu, Y. Jiang, Y. P. Feng, M. Yang and S. Wang, *J. Alloys Compd.*, 2022, **893**, 162223.
13 X.-J. Dong, J.-Y. You, B. Gu and G. Su, *Phys. Rev. Appl.*, 2019, **12**, 014020.
14 A. A. Bukharaev, A. K. Zvezdin, A. P. Pyatakov and Y. K. Fetisov, *Phys.-Usp.*, 2018, **61**, 1175–1212.
15 F. Miao, S.-J. Liang and B. Cheng, *npj Quantum Mater.*, 2021, **6**, 59.
16 C. Gong, L. Li, Z. Li, H. Ji, A. Stern, Y. Xia, T. Cao, W. Bao, C. Wang, Y. Wang, Z. Q. Qiu, R. J. Cava, S. G. Louie, J. Xia and X. Zhang, *Nature*, 2017, **546**, 265–269.
17 B. Huang, G. Clark, E. Navarro-Moratalla, D. R. Klein, R. Cheng, K. L. Seyler, D. Zhong, E. Schmidgall, M. A. McGuire, D. H. Cobden, W. Yao, D. Xiao, P. Jarillo-Herrero and X. Xu, *Nature*, 2017, **546**, 270–273.
18 C. Gong and X. Zhang, *Science*, 2019, **363**, 706.
19 H. González-Herrero, J. M. Gómez-Rodríguez, P. Mallet, M. Moaied, J. J. Palacios, C. Salgado, M. M. Ugeda, J.-Y. Veuillen, F. Yndurain and I. Brihuega, *Science*, 2016, **352**, 437–441.
20 J. Jung, T. Pereg-Barnea and A. H. Macdonald, *Phys. Rev. Lett.*, 2009, **102**, 227205.
21 O. V. Yazyev and M. I. Katsnelson, *Phys. Rev. Lett.*, 2008, **100**, 047209.
22 Z. Zhang, X. Zou, V. H. Crespi and B. I. Yakobson, *ACS Nano*, 2013, **7**, 10475–10481.
23 T. Cao, Z. Li and S. G. Louie, *Phys. Rev. Lett.*, 2015, **114**, 236602.
24 P. Wei, S. Lee, F. Lemaitre, L. Pinel, D. Cutaia, W. Cha, F. Katmis, Y. Zhu, D. Heiman, J. Hone, J. S. Moodera and C. T. Chen, *Nat. Mater.*, 2016, **15**, 711–716.
25 Z. Wang, C. Tang, R. Sachs, Y. Barlas and J. Shi, *Phys. Rev. Lett.*, 2015, **114**, 016603.
26 S.-H. Zhang and B.-G. Liu, *J. Mater. Chem. C*, 2018, **6**, 6792–6798.
27 Z. Chen, J. He, P. Zhou, J. Na and L. Z. Sun, *Comput. Mater. Sci.*, 2015, **110**, 102–108.
28 X. Hu, Y. Zhao, X. Shen, A. V. Krasheninnikov, Z. Chen and L. Sun, *ACS Appl. Mater. Interfaces*, 2020, **12**, 26367–26373.
29 J. Zhou, X. Song, M. Yang, J. Chai, N. L. M. Wong, L. Shen, S. Wang and Y. P. Feng, *J. Mater. Chem. C*, 2021, **9**, 16576–16580.
30 G. Kresse and J. Hafner, *Phys. Rev. B: Condens. Matter Mater. Phys.*, 1993, **47**, 558–561.
31 G. Kresse and J. Hafner, *Phys. Rev. B: Condens. Matter Mater. Phys.*, 1994, **49**, 14251–14269.
32 G. Kresse and D. Joubert, *Phys. Rev. B: Condens. Matter Mater. Phys.*, 1999, **59**, 1758–1775.
33 S. Grimme, J. Antony, S. Ehrlich and H. Krieg, *J. Chem. Phys.*, 2010, **132**, 154104.
34 A. Jain, S. P. Ong, G. Hautier, W. Chen, W. D. Richards, S. Dacek, S. Cholia, D. Gunter, D. Skinner, G. Ceder and K. A. Persson, *APL Mater.*, 2013, **1**, 011002.
35 A. Togo and I. Tanaka, *Scr. Mater.*, 2015, **108**, 1–5.
36 A. A. Mostofi, J. R. Yates, Y.-S. Lee, I. Souza, D. Vanderbilt and N. Marzari, *Comput. Phys. Commun.*, 2008, **178**, 685–699.
37 V. V. Mazurenko, A. N. Rudenko, S. A. Nikolaev, D. S. Medvedeva, A. I. Lichtenstein and M. I. Katsnelson, *Phys. Rev. B*, 2016, **94**, 214411.
38 I. V. Solovyev, Z. V. Pchelkina and V. V. Mazurenko, *CrystEngComm*, 2014, **16**, 522–531.
39 X.-L. Fan, Y. Yang, P. Xiao and W.-M. Lau, *J. Mater. Chem. A*, 2014, **2**, 20545–20551.
40 B. C. McCollum, D. S. Dudis, A. Lachgar and J. D. Corbett, *Inorg. Chem.*, 1990, **29**, 2030–2032.
41 M. Ashton, J. Paul, S. B. Sinnott and R. G. Hennig, *Phys. Rev. Lett.*, 2017, **118**, 106101.
42 N. Mounet, M. Gibertini, P. Schwaller, D. Campi, A. Merkys, A. Marrazzo, T. Sohier, I. E. Castelli, A. Cepellotti, G. Pizzi and N. Marzari, *Nat. Nanotechnol.*, 2018, **13**, 246–252.

43 J. Feng, X. Sun, C. Wu, L. Peng, C. Lin, S. Hu, J. Yang and Y. Xie, *J. Am. Chem. Soc.*, 2011, **133**, 17832–17838.
44 Y. Ma, Y. Dai, M. Guo, C. Niu, Y. Zhu and B. Huang, *ACS Nano*, 2012, **6**, 1695–1701.
45 E. C. Stoner, *Proc. R. Soc. London, Ser. A*, 1938, **165**, 372–414.
46 J. C. Slater, *Phys. Rev.*, 1930, **35**, 509–529.
47 J. C. Slater, *Phys. Rev.*, 1930, **36**, 57–64.
48 G. Stollhoff, A. M. Oles and V. V. Heine, *Phys. Rev. B: Condens. Matter Mater. Phys.*, 1990, **41**, 7028–7041.
49 M. I. Katsnelson, V. Y. Irkhin, L. Chioncel, A. I. Lichtenstein and R. A. de Groot, *Rev. Mod. Phys.*, 2008, **80**, 315–378.
50 M. Jourdan, J. Minar, J. Braun, A. Kronenberg, S. Chadov, B. Balke, A. Gloskovskii, M. Kolbe, H. J. Elmers, G. Schonhense, H. Ebert, C. Felser and M. Klaui, *Nat. Commun.*, 2014, **5**, 3974.
51 S. A. Wolf, D. D. Awschalom, R. A. Buhrman, J. M. Daughton, S. von Molnar, M. L. Roukes, A. Y. Chtchelkanova and D. M. Treger, *Science*, 2001, **294**, 1488–1495.
52 J. N. Coleman, M. Lotya, A. O'Neill, S. D. Bergin, P. J. King, U. Khan, K. Young, A. Gaucher, S. De, R. J. Smith, I. V. Shvets, S. K. Arora, G. Stanton, H. Y. Kim, K. Lee, G. T. Kim, G. S. Duesberg, T. Hallam, J. J. Boland, J. J. Wang, J. F. Donegan, J. C. Grunlan, G. Moriarty, A. Shmeliov, R. J. Nicholls, J. M. Perkins, E. M. Grieveson, K. Theuwissen, D. W. McComb, P. D. Nellist and V. Nicolosi, *Science*, 2011, **331**, 568–571.
53 X. Fan, P. Xu, D. Zhou, Y. Sun, Y. C. Li, M. A. Nguyen, M. Terrones and T. E. Mallouk, *Nano Lett.*, 2015, **15**, 5956–5960.
54 M. M. Ugeda, I. Brihuega, F. Guinea and J. M. Gomez-Rodriguez, *Phys. Rev. Lett.*, 2010, **104**, 096804.
55 Z. Hu, Z. Wu, C. Han, J. He, Z. Ni and W. Chen, *Chem. Soc. Rev.*, 2018, **47**, 3100–3128.
56 P. K. J. Wong, W. Zhang, J. Zhou, F. Bussolotti, X. Yin, L. Zhang, A. T. N'Diaye, S. A. Morton, W. Chen, J. Goh, M. P. de Jong, Y. P. Feng and A. T. S. Wee, *ACS Nano*, 2019, **13**, 12894–12900.
57 Z. Shao, Z. G. Fu, S. Li, Y. Cao, Q. Bian, H. Sun, Z. Zhang, H. Gedeon, X. Zhang, L. Liu, Z. Cheng, F. Zheng, P. Zhang and M. Pan, *Nano Lett.*, 2019, **19**, 5304–5312.
58 Y. Huang, Y. H. Pan, R. Yang, L. H. Bao, L. Meng, H. L. Luo, Y. Q. Cai, G. D. Liu, W. J. Zhao, Z. Zhou, L. M. Wu, Z. L. Zhu, M. Huang, L. W. Liu, L. Liu, P. Cheng, K. H. Wu, S. B. Tian, C. Z. Gu, Y. G. Shi, Y. F. Guo, Z. G. Cheng, J. P. Hu, L. Zhao, G. H. Yang, E. Sutter, P. Sutter, Y. L. Wang, W. Ji, X. J. Zhou and H. J. Gao, *Nat. Commun.*, 2020, **11**, 2453.
59 Y. Wang, C. Wang, S. J. Liang, Z. Ma, K. Xu, X. Liu, L. Zhang, A. S. Admasu, S. W. Cheong, L. Wang, M. Chen, Z. Liu, B. Cheng, W. Ji and F. Miao, *Adv. Mater.*, 2020, **32**, e2004533.
60 M. M. Salary, S. Inampudi, K. Zhang, E. B. Tadmor and H. Mosallaei, *Phys. Rev. B*, 2016, **94**, 235403.
61 G. H. Ahn, M. Amani, H. Rasool, D. H. Lien, J. P. Mastandrea, J. W. Ager Iii, M. Dubey, D. C. Chrzan, A. M. Minor and A. Javey, *Nat. Commun.*, 2017, **8**, 608.
62 R. Frisenda, M. Drüppel, R. Schmidt, S. Michaelis de Vasconcellos, D. Perez de Lara, R. Bratschitsch, M. Rohlfing and A. Castellanos-Gomez, *npj 2D Mater. Appl.*, 2017, **1**, 10.
63 F. Guo, Y. Lyu, M. B. Jedrzejczyk, Y. Zhao, W. F. Io, G. Bai, W. Wu and J. Hao, *Appl. Phys. Lett.*, 2020, **116**, 113101.